NMR Imaging of Morphology, Defects, and Composition of Tire Composites and Model Elastomer Blends

Subhendra N. Sarkar and Richard A. Komoroski*

Departments of Radiology and Pathology, University of Arkansas for Medical Sciences, 4301 West Markham Street, Little Rock, Arkansas 72205

Received July 11, 1991

ABSTRACT: Multiple-slice, three-dimensional (3D) ^{1}H NMR imaging at medium resolution (100–200 μm) and short echo times (0.5–2 ms) has been used to visualize the elastomeric components of several tire sections. The various rubber layers and cords were readily distinguished for a non-steel-belted tire section at 200-μm resolution, presumably based on T_2 differences among the different components. Carbon-13 magic angle spinning NMR of samples from each layer provided elastomer composition, which supported the origin of the intensity differences seen by NMR imaging. The ability to detect small differences of composition in actual tires was confirmed by imaging well-characterized diblends of *cis*-polybutadiene (BR) and styrene–butadiene rubbers (SBR). From T_2-weighted images or from the total intensity profiles, a 20% difference in blend composition was distinguished. Experimental tire tread sections with good and poor carbon black dispersions produced substantially different images at 150-μm in-plane resolution. Artifactual intensity patterns from bulk magnetic susceptibility differences between certain defects and the elastomer matrix were observed in some of the samples and may be useful for defect identification.

Introduction

Nuclear magnetic resonance (NMR) imaging is a promising tool for nondestructive mapping of spatial structures in materials.[1] Currently, only relatively concentrated constituents with high molecular mobility are routinely imageable. This includes low-molecular-weight diffusants in polymers[2,3] or porous materials,[4,5] polymeric binders in green ceramics,[6] and elastomeric materials well above their T_g.[7-10]

A major focus of NMR imaging research is currently on difficult-to-image rigid materials. Glassy or crystalline materials have very short transverse spin relaxation times (T_2) and large line widths and require experimentally demanding line-narrowing methods in conjunction with imaging techniques.[11,12] Magic angle spinning (MAS) combined with imaging techniques[13] is possible but seems impractical for large or irregular industrial samples. The use of mobile penetrants in rigid materials or rubbers can improve the ability to obtain images. However, this may create differential swelling and local dimensional changes that make interpretation of such images problematic.

Image-guided localized ^{1}H spectroscopy[14] can potentially provide information on molecular composition for regions of several cubic millimeters in samples of high molecular mobility. However, in materials ^{1}H lines are broad and unresolved, making localized ^{1}H spectroscopy an unattractive choice.[15]

To date no study has appeared using NMR imaging to detect variations in composition of tire composites and elastomeric blends. Such materials have moderately narrow NMR lines (300–1000 Hz) due to polymer chain segmental motions,[15] with ^{1}H T_2s typically in the range of 0.5–5 ms which is beyond the range of echo times (TE) available on medical imagers.[7]

One approach to characterize materials of this type is to stretch the current limitations of medical NMR imaging by employing strong, actively shielded gradients capable of fast switching (50–100 μs) and submillisecond TEs and intermediate-size magnet bores (10–25 cm) capable of accommodating a wider range of samples than standard high-resolution NMR systems. We have used a modified, three-dimensional (3D) volume imaging approach[16] to achieve short TEs (<1 ms), practical image resolutions (100–200 μm) close to the predicted limits for elastomer line widths,[7] and contiguous multislice images of whole samples in a few minutes to a few hours. This work emphasizes development of NMR imaging as a nondestructive mapping technique sensitive to blend composition, filler dispersion, curing, and defects in filled, cured elastomers as a continuation of previous work.[7,8,17]

We report here NMR images of several tire sections which demonstrate visualization of composite elastomeric layers of varying composition, tire cords, and differences in dispersion of carbon black in finished tire tread. Images of model diblends yield an estimate of the sensitivity of the technique to elastomer compositional changes. Finally, abrupt changes in magnetic susceptibility at defect interfaces can create shape and intensity artifacts in NMR images.[18,19] We report the observation of such artifacts in filled elastomers.

Experimental Section

Samples. For imaging studies, sections about 10 mm × 10 mm square and 4 mm thick from three finished tires were taken. One sample consisted of a transverse cross section of a small, non-steel-belted bias-ply tire. In addition, tread samples were cut from sections of two experimental steel-belted, radial automobile tires specially prepared with treads having good and poor dispersion of carbon black, as measured by the AMEDA (Automatic Microscope Electronic Data Accumulator) technique.[20]

In addition, a set of eight well-characterized elastomer samples was studied. The set consisted of uncured, unfilled *cis*-polybutadiene (*cis*-BR) and emulsion styrene–butadiene (SBR; 23.5% styrene) rubbers and six 2-mm-thick sheets of cured (at 160 °C for 20–25 min) and filled (60 phr carbon black) diblends with *cis*-BR/SBR compositions of 100:0, 80:20, 60:40, 40:60, 20:80, and 0:100 by weight. Other initial components before cure included 15% processing oil, 0.9% stearic acid, 2% antiozonant, 2% tackifier, 2% antioxidant, 3% zinc oxide, 1.7% sulfur, and 1.5% accelerator. The processing oil is largely volatilized in the curing process. Images were obtained for the blend sheets cut to a size of 2 × 4 × 10 mm^3. The 10-mm-long and 2-mm-thick edges were laid with fixed spacing between the individual sheets in the plane (*xz* plane of the magnet) by means of glass spacers.

Finally, a phantom was prepared with "defects" of known geometry and bulk magnetic susceptibility differences by em-

* To whom all correspondence should be addressed.

0024-9297/92/2225-1420$03.00/0

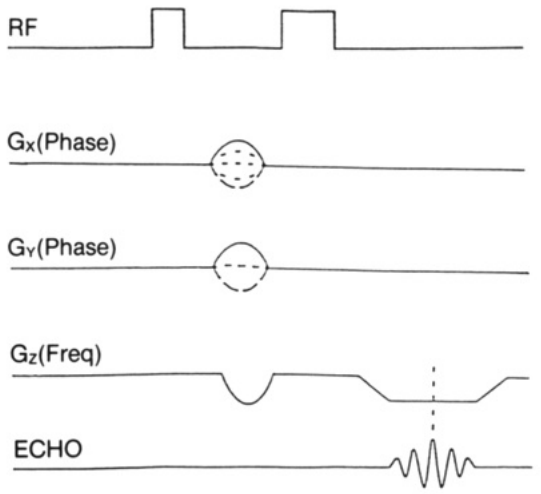

Figure 1. Schematic diagram of the 3D whole volume imaging sequence used to acquire images in the text. Slice selection was done by phase encoding in the y direction.

bedding an air-filled glass capillary tube, a carbon-black-filled glass capillary, and a graphite pencil tip in a matrix of commercial vegetable shortening (Crisco, Proctor and Gamble Co.) contained in a glass vial. Carbon black was also mixed directly into a region of the vegetable shortening.

3D Imaging at 4.7 T. A General Electric Omega CSI 4.7-T system with Acustar shielded gradients and a maximum gradient strength of 20 G/cm in a 120-mm magnet bore was used to image ^{1}H at 200.1 MHz. Samples were imaged with a single-turn, 2-cm ^{1}H surface coil for both excitation and detection. The positioning and size of the samples relative to the surface coil were such that the radio-frequency field inhomogeneities over the volume of the sample examined were minimal.

The 3D volume imaging pulse sequence shown in Figure 1 was employed for obtaining contiguous multislices to cover the entire volume of the samples. In this sequence, a rectangular 90° pulse of 17–20-μs duration was applied to excite the entire sample. Phase encoding was done by stepping gradients (one-lobe sinusoidal, 20 G/cm, 250–300-μs duration) 128 and 16 times, respectively, in the x and y directions. The frequency encoding gradient (z direction) was about 10 G/cm. A maximum digitizing rate of 200 kHz (128 points) was used to minimize the acquisition time. Crusher gradients were not required. The echo times were 0.5–2 ms for in-plane resolutions from 400 × 400 to 100 × 100 μm^2. Slice thicknesses were typically 0.2–0.5 mm. The sum of the intensities along the phase-encode direction for the diblend sheet sample was obtained by turning off the phase-encode gradients at TEs ranging from 0.5 to 6 ms.

The spin–lattice relaxation times (T_1) of the broad ^{1}H peak for each of the tire sections, for the six blend sheets together, and for each of the sheets separately were measured by the inversion–recovery method and the T_2 values by the Hahn spin-echo technique at 4.7 T.

Spectroscopy at 7.05 T. Mobile ^{1}H contents for all samples were determined by integrating the peak intensities of ^{1}H spectra at 300.5 MHz (pw 6.8 μs, tip angle 90°, single scan) on a General Electric GN-300WB spectrometer at 19 °C in 5-mm NMR tubes. The values were normalized with respect to that of cured 100:0 *cis*-BR/SBR. The ^{13}C MAS NMR spectra were obtained at 75.57 MHz (pw 7.8 μs, tip angle 38°, repetition time 2 s) from about 0.5 g of finely cut rubber pieces from various layers of the non-steel-belted tire in a Chemagnetics MAS accessory employing 9-mm rotors at about a 400-Hz spinning rate with pulse-modulated low-power ^{1}H decoupling at 20 °C. No serious attempt was made to quantitate the ^{13}C MAS spectra.

Results and Discussion

The details of the modified 3D imaging sequence[16] have been described in the Experimental Section. Advantages of this sequence are (1) short echo times, (2) nonoverlapping, contiguous slices of the entire sample, and (3) a large excitation bandwidth resulting from narrow radio-frequency pulses. The major disadvantage for imaging whole volumes of large samples is that high isotropic resolution requires long data acquisition times and processing of large data sets. Crusher gradients are commonly inserted into imaging pulse sequences to destroy residual, unwanted transverse magnetization from pulse imperfections that can produce image artifacts. We found such crusher gradients to be unnecessary here, presumably because such residual transverse magnetization is short-lived for the short-T_2 samples examined.

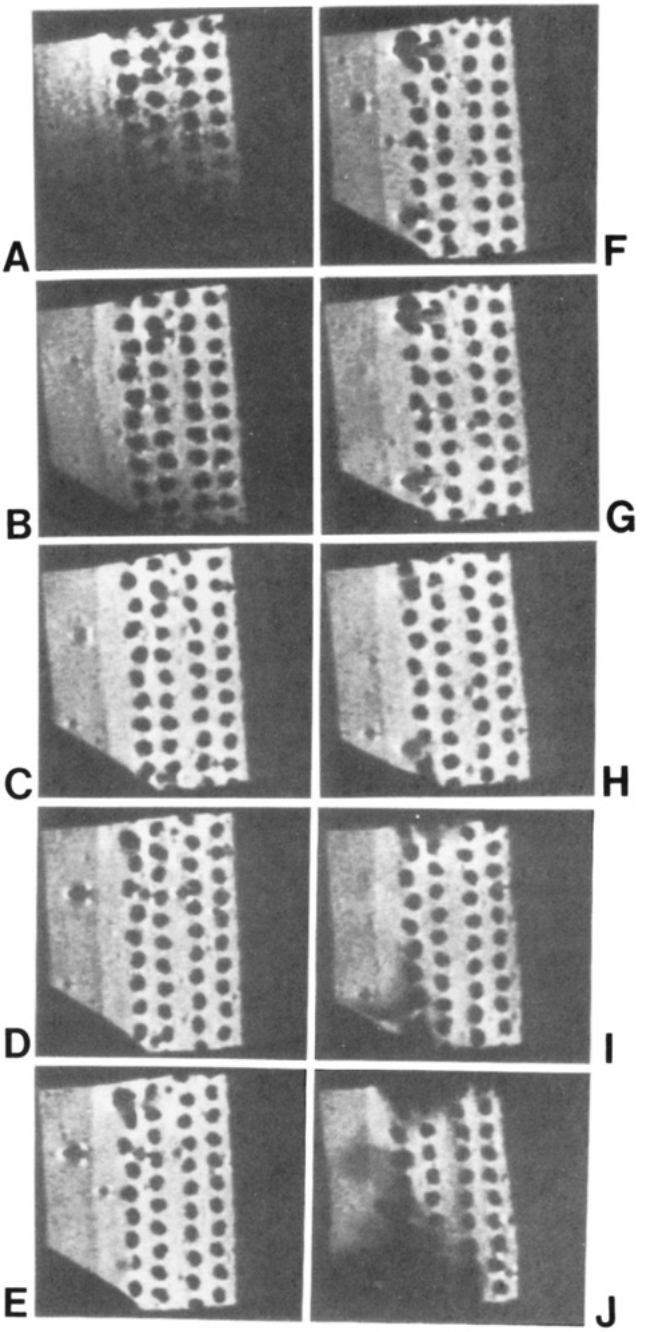

Figure 2. Ten image slices (200 μm thick; FOV 9 mm) (A–J) of 100-μm in-plane resolution covering the entire volume of a cross section of a non-steel-belted tire. TE, 1.9 ms; TR, 1 s; total time, 2 h; data size, 128 × 128 × 16. Here slice A was closest to the radio-frequency coil, and the image intensity was manually adjusted for uniformity among the slices.

3D NMR Imaging and ^{13}C NMR of a Tire Section. Figure 2 shows 10 (from a set of 16) contiguous transverse slices, each 200 μm thick, of a 3D NMR image at a TE of 1.9 ms covering the entire volume of the non-steel-belted

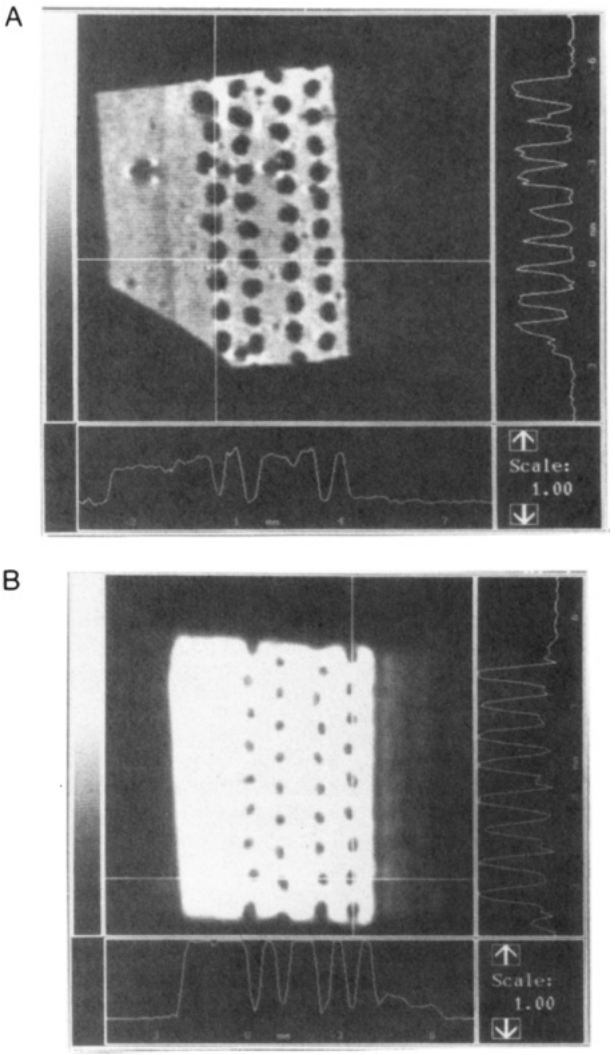

Figure 3. (A) Expansion of the image in Figure 2D. (B) 500-μm slice (TE; 750 μs) centered at the same plane as that of Figure 2D at 200-μm in-plane resolution with the intensity burned-in to highlight the presence of two weak layers on the right.

tire cross section. The tread is to the left and the interior portion of the tire to the right. At the in-plane resolution of 100 μm, the tread layer at the left can be distinguished from the second region of higher intensity containing embedded rigid fibers appearing as dark spots in each slice. The layer boundary as well as the fiber–rubber interfaces is well-defined. In the T_2-weighted images, the fibers yield no signal because of very short T_2 associated with the absence of substantial molecular motion. Visual examination of the tire cross section and the cord placement reveals that a region to the right of the cords is not appearing in Figure 2. A 2-mm-thick layer, which visually appears no different from the leftmost layer, is barely visible on the right. Numerous other defects, presumably voids, chunks of carbon black or other material, and broken or misaligned fibers are also present in these images. The 3D structure of the various defects is well-defined in this set of contiguous, reasonably thin slices. Some of the defects display a characteristic arrowhead pattern[19] of bright spots pointing along the frequency encode direction. This pattern results from magnetic susceptibility differences between the defect and the surrounding matrix and is described in more detail later.

Figure 3A shows the same slice as in Figure 2D, expanded to reveal more details. The rightmost layer mentioned above is barely visible in the image and profile (at the bottom in Figure 3A), which are suggestive of two layers in this region. Figure 3B is an image of a 500-μm slice centered at the same plane as that of Figure 2D. Here the TE has been shortened to 750 μs, with the accompanying loss in resolution (200 × 200 × 500 μm). The image has been burned-in to clearly show the presence of the rightmost layer, which is more clearly defined as two layers in the profile at the bottom. The combination of shorter TE and coarser resolution has enhanced the visibility of this feature. The result in Figure 3 demonstrates the advantage of submillisecond TE for observing structures in spin-echo images of elastomeric products. The two-layer nature of the rightmost region was not visually apparent and is a feature detectable perhaps only by NMR imaging.

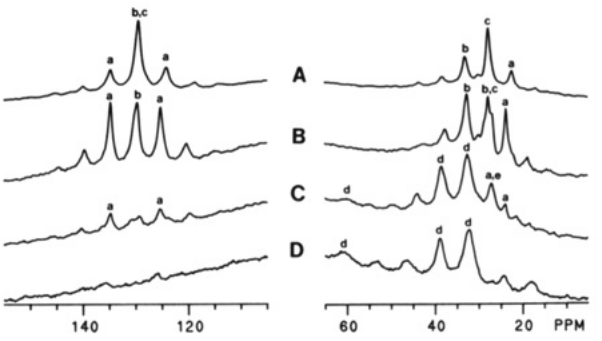

Figure 4. ^{13}C scalar-decoupled MAS spectra at 75.57 MHz and a spin rate of about 400 Hz. (A) Sample from the outermost layer (tread) of a tubeless tire. (B) Sample from the middle region including rigid fibers. (C) Sample from the left of the two rightmost inner layers. (D) Sample from the innermost layer on the right. Peaks are from NR (a), *cis*-BR (b), SBR (c), butyl rubber (d), and spinning sideband (e).

Intensity differences in T_2-weighted NMR images of previously uncharacterized finished products, such as the tire section shown here, may arise from several sources, including differences in rubber content, composition, filler, and cure for example. A complete chemical and morphological characterization of the tire section in question is beyond the scope of this work. However, a limited analysis of the elastomer composition of the various layers has been performed to provide a likely rationalization of the intensity variations among layers in Figures 2 and 3.

Figure 4 shows four scalar-decoupled ^{13}C MAS spectra at 75.57 MHz corresponding to sample A, the outermost layer (tread), sample B, the middle layer containing fibers, sample C, the layer immediately adjacent to B on the right, and sample D, the interior layer (closest to the enclosed air in a tubeless tire). These are ordered from left to right in Figures 2 and 3. The major peaks in all four spectra can tentatively be identified by comparison to high-resolution ^{13}C NMR spectra of common elastomers and blends.[21] Assignments are given in the caption to Figure 4. Peaks not assigned are spinning sidebands of the major resonances or unidentified minor structures. Figure 4D corresponds to primarily butyl rubber[21] (peaks marked d). Figure 4C shows the presence of a small amount of *cis*-polyisoprene or natural rubber (NR; peaks marked a) blended with butyl rubber. A spinning sideband (e), identified by varying the spin rate, overlaps one of the NR peaks. Spectra A and B in Figure 4 correspond to NR/*cis*-BR/SBR blends (peaks indicated by a–c, respectively) in the ratios of roughly 20:10:70 and 40:10:50, respectively. There is substantial ambiguity in the *cis*-BR/SBR ratios due to overlap of butadiene peaks.[21]

The tread layer has a lower intensity than the middle layer presumably due to its relatively higher amount of SBR and lower amount of NR. The innermost double

Table I
NMR Relaxation Times, Relative ^1H Contents, and Linewidths of Actual and Experimental Tire Tread Sections

tire sample	rel ^1H content	line width, Hz	T_1, ms	T_2, μs
bias-ply tire section		1850	410	<100,[a] 950
exptl tread, poor dispersion of carbon black	0.85	2600	450	(60%), 1000 (40%), 630
exptl tread, good dispersion of carbon black	1.00	1400	380	1100

[a] Minor component of T_2 responsible for 10% of the total intensity.

layer of greatly reduced intensity on the NMR images contains primarily butyl rubber. Butyl rubber is commonly used as an air barrier on the inner surface of tubeless tires. Although the T_g of polyisobutylene (and butyl rubber) is −70 °C, its polymer chain segmental mobility is substantially restricted relative to elastomers of similar T_g, as has been demonstrated previously by ^{13}C spin relaxation measurements.[22] Thus, with a shorter ^1H T_2 (<0.1 ms) than other common elastomers, butyl rubber is more difficult to detect in NMR images. The addition of some *cis*-polyisoprene rubber (natural or synthetic) would increase the ^1H T_2 of that layer, making it slightly more intense on the NMR image. The subtle difference in composition in the butyl-rubber-containing portion of this cross section is the type of feature that may only be discernable by NMR imaging, through its sensitivity to molecular composition via the dependence of spin relaxation on molecular mobility.

The image-guided destructive analysis by ^{13}C MAS NMR can offer further information supporting the nondestructive and quick observation available through NMR imaging. Bulk spectral or spin relaxation measurements obviously cannot provide the spatial detail nondestructively. The detailed composite nature of the tire tread as a whole is completely obscured in the measured values of ^1H NMR relaxation parameters and line widths given in Table I.

NMR Imaging of *cis*-BR/SBR Model Diblends. Application of NMR imaging to nondestructive characterization of material composition, particularly for composite elastomer systems, may require some type of calibration curve from the images of simpler, well-characterized components which comprise the whole composite system. Imaging of *cis*-BR/SBR diblends of known composition can demonstrate such an approach for an important class of elastomeric composites.

Six model sheets of *cis*-BR/SBR have been studied in detail. Relaxation parameters and line widths for each of the sheets and for the combined stack of all sheets are given in Table II. The increase in T_1 values with increasing SBR content is slight. For each of the blend sheets there was a short T_1 component (not given here) contributing about 10% of the total intensity, perhaps due to bound polymer on carbon black particles. Similarly, the change in line width with increasing SBR content tells little about the blends.

On the other hand, T_2 decreases steadily and substantially with increasing SBR content, which is a consequence of the decreased low-frequency segmental mobility of SBR (T_g of SBR = −55 °C; T_g of *cis*-BR = −102 °C). For each of the sheets there was a minor, long component of T_2 responsible for the residual intensity that permitted imaging at much longer TEs. The origin of this long component may be intrinsic nonexponentiality of the relaxation process or traces of residual processing oil.

Table II
NMR Relaxation Times, Line Widths, and Relative ^1H Contents of *cis*-BR, SBR, and the Model Diblends at 4.7 T

compn (cured, filled *cis*-BR:SBR wt %)	rel ^1H content	approx line widths	T_1, ms	T_2, μs
pure *cis*-BR		150	330	1100, 4000[a]
pure SBR		550	440	500, 6000[a]
100:0	1.00	650	270	1000
80:20	1.07	600	300	880
60:40	1.02	650	320	730
40:60	1.01	750	330	620
20:80	1.00	820	370	500
0:100	0.92	980	440	50–150
six sheets together		1200	420	750

[a] Minor component of T_2 responsible for 10% of the total intensity.

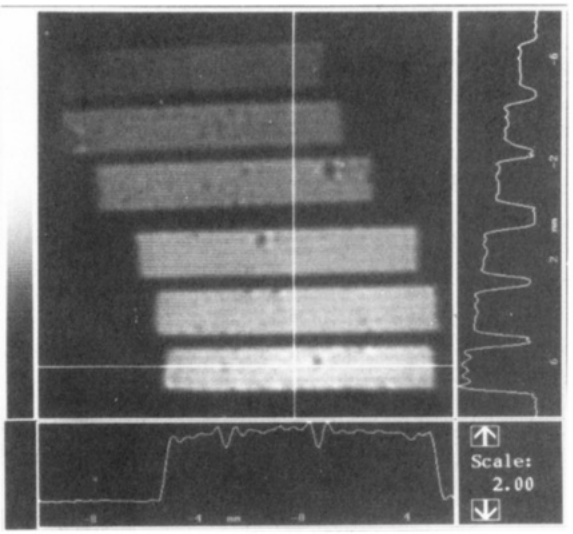

Figure 5. 500-μm slice from a 16-slice volume data set of six model diblend sheets of *cis*-BR/SBR with composition ratios 100:0, 80:20, 60:40, 40:60, 20:80, and 0:100 (bottom to top) at 200-μm in-plane resolution. TE, 1.1 ms; TR, 1 s; total time, 1 h.

The relative uniformity in ^1H density for these sheets (Table II) leaves the variation in T_2 as the prime cause of the image and profile intensity variations (see below). Under our pulsing conditions, the small range of T_1 of the sheets results in a very slight T_1 dependence, less than the variation in ^1H density. Note that measurement of any of the above NMR parameters on the stack of all six sheets tells very little about local composition variations in the composite.

Figure 5 shows a typical NMR image from a 16-slice, 3D dataset with 200 × 200 × 500 μm^3 resolution for the six model *cis*-BR/SBR blend sheets at a TE of 1.1 ms. As the SBR content increases, the image intensity decreases as expected in regular fashion, which is also evident in the image profile on the right side. The results in Figure 5 demonstrate the ability of NMR imaging to exquisitely differentiate polymer blend compositions based on T_2 differences. The degree of differentiation depends on the variation in T_2 and the TE used. In this case the T_2 variation was at least 100 μs (10% of the TE used) between two adjacent sheets having a 20% difference in SBR content. Perhaps as little as a 10% variation in composition could be detected.

Figure 6 shows image profiles of the same stack of sheets at TE = 6, 1, and 0.5 ms. Clearly the use of a very short TE brings about a substantial improvement in our ability to detect the high-SBR-content sheets as it did for the butyl rubber layers of the tire section. However, as expected, we are not able to remove the effect of T_2 for

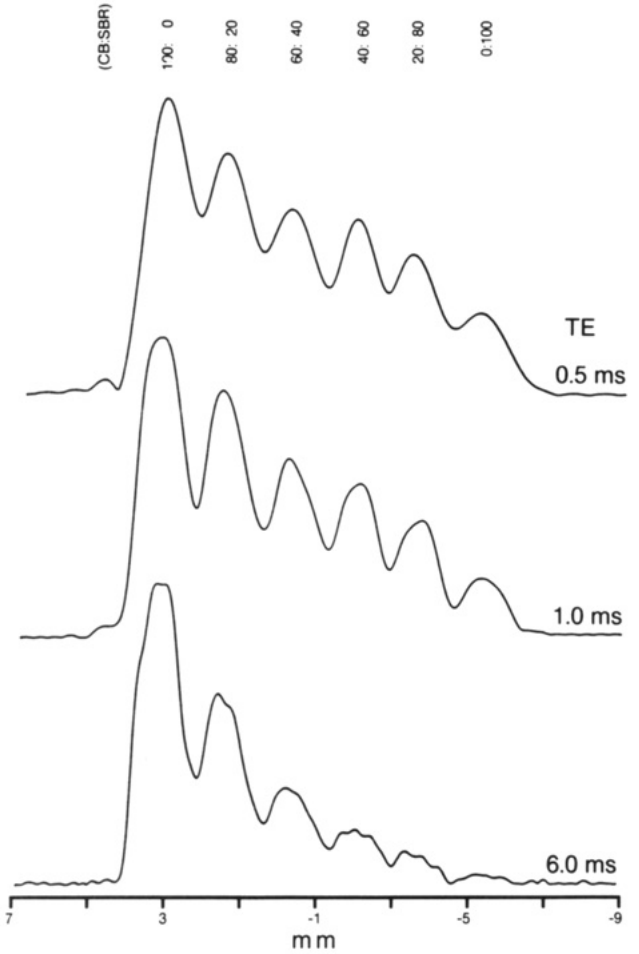

Figure 6. Summed intensity profiles from the *cis*-BR/SBR diblend sheets at TE 6, 1, and 0.5 ms. TR, 5 s; total time, 9 min.

these typical elastomers even at a TE of 0.5 ms. In a T_2-independent profile, all six peaks would be of approximately equal intensity, as indicated by the results in the second column of Table II. Lowering the TE by a factor of 2–4 from 0.5 ms, as might be achieved by stronger gradients and a faster digitizer, will not radically improve our ability to image submillisecond T_2 materials such as butyl rubber and polychloroprene. At least a 10-fold reduction in TE is needed to obtain T_2-independent images of most common cured and filled elastomers.

An alternative might be to employ line-narrowing pulse sequences used for rigid materials.[11,12] However, it is not clear how effective line-narrowing sequences will be for elastomers, where the dipolar line width is strongly narrowed by chain segmental motion.[15] In such a case, the characteristic frequency of the line-narrowing sequence must exceed the frequency of the segmental motion, which corresponds to a correlation time of about 10^{-8} s. In this case the only alternative is to increase the temperature of the sample.[23] Nevertheless, although T_2-independent images cannot be obtained using the methods employed here, high-quality images sensitive to elastomer composition are possible.

Carbon Black Dispersion. The mechanical properties of a tire tread depend strongly on the degree of carbon black dispersion, among other things. A tire tread in which the carbon black is not well-dispersed displays inferior performance. Carbon black dispersion is typically measured at the surface by mechanical[24] or photometric techniques such as AMEDA.[20] There is no nondestructive way to characterize carbon black dispersion locally within a sample.

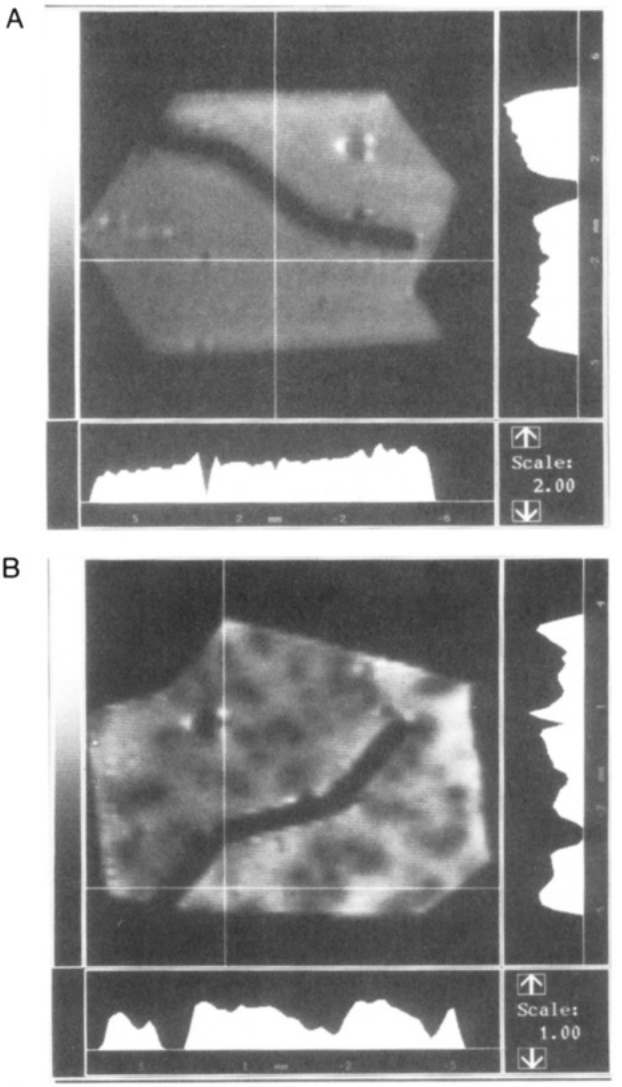

Figure 7. (A) Typical NMR image from an experimental tire tread with a good dispersion of carbon black at 150 × 150 × 350 μm^3 resolution. Total time, 2 h. (B) NMR image of an experimental tire tread with a poor carbon black dispersion. TE, 1.3 ms; TR, 1 s for both.

Figure 7 shows typical images from two finished tire tread sections—one with good and the other with poor carbon black dispersion. Tread grooves are well-defined in both sections. The relatively even appearance in Figure 7A is consistent with well-dispersed carbon black, although the section is not defect-free. The image of Figure 7B displays a highly uneven appearance, consisting of regions of poor dispersion of several hundred microns diameter detectable at 150-μm in-plane resolution. The S/N ratio is generally lower for the tread with a poor dispersion, even though the imaging time was 5 times longer than that with the good dispersion. A substantial fraction of the NMR intensity is lost apparently due to the heterogenous nature of the sample with a poor carbon black dispersion. Note that the T_2 measurements on the sections gave two values of T_2 for the poor dispersion sample, as compared to a single value of T_2 for the good dispersion sample (Table I). A fraction of polymer in the poor dispersion section has a substantially reduced T_2, resulting in a signal loss at constant TE. This fraction may represent bound rubber. This is another example where the two results together provided more information than NMR imaging or relaxation parameters alone.

Magnetic Susceptibility Artifacts in NMR Images. In most of the images shown above, defects surrounded

by three bright spots in an arrowhead configuration appear in the frequency encode direction. Frequency shifts of a compartmentalized nucleus[18] as well as the resulting field distortions[19] due to interfacial magnetic susceptibility differences and compartment geometry can produce artifactual intensity patterns similar to those observed here. Such artifacts have been described in detail elsewhere.[19] In addition to depending on the size and shape of the object, these distortions are proportional to the magnetic susceptibility difference across the interface and the static magnetic field strength and inversely proportional to the strength of the frequency encode gradient.[19] Their direction reverses upon changing the gradient direction, which we have confirmed here in one case.

Since this pattern is common in the NMR images of carbon-black-filled elastomers, it is important to identify the source(s). Among the possibilities are voids, particles of metal or other foreign material, or agglomerates of carbon black. We suspect that the artifacts arise from relatively large particles of crystalline, graphitic carbon black ("coke") which are usually present in the unmixed carbon black and are produced in the carbon black manufacturing process.[25] The location and size of such particles are important in that they can serve as initial points for failure under stress or in service.[25]

This undesirable component could result in a large magnetic susceptibility difference relative to the surrounding filled elastomer. As a crude test of this hypothesis, Figure 8A shows a typical volume image of a phantom consisting of a glass capillary filled with air (top right), another glass capillary filled with powdered carbon black (close to center), and a graphite pencil tip (lower center) embedded in a matrix of commercial vegetable shortening. Additional irregular air pockets are also visible. About a third of the total volume of this matrix at the top was mixed directly with about 1 g of powdered carbon black.

No prominent magnetic susceptibility artifacts are seen at any of the air pockets or either glass capillary. A prominent arrowhead artifact appears only at the graphite tip. Figure 8B shows the gradient-recalled-echo image of the same slice. In this sequence the read gradient polarity is reversed to refocus the spins, instead of a 180° pulse.[7] Such images are generally sensitive to T_2*, the time constant for decay of the free induction signal. Defects can appear magnified in such images if a magnetic susceptibility difference produces reduced T_2* near the defect surface.[7] Note that the arrowhead pattern is washed away and the feature from the pencil tip greatly enlarged. Most of the other defects undergo no or minimal enlargement. No evidence is seen in either image in Figure 8 for the directly mixed carbon black.

The above results support our interpretation of the NMR origin of the artifacts. "Coke" particles are the most likely cause, although small iron or rust particles or perhaps particulate carbon black agglomerates cannot be ruled out totally. In one case of a carbon-black-filled, uncured elastomer where the artifacts were seen, a search for metal particles was unsuccessful. Artifacts such as these can complicate interpretation of NMR images. However, one may be able to identify impurities or defects based on susceptibility artifacts, a point worthy of further study.

Conclusions

We have shown that direct T_2-weighted, low-TE spin-echo NMR imaging can visualize certain morphologic and defect structures and can differentiate among various layers in actual tire samples with no probing agent. At a

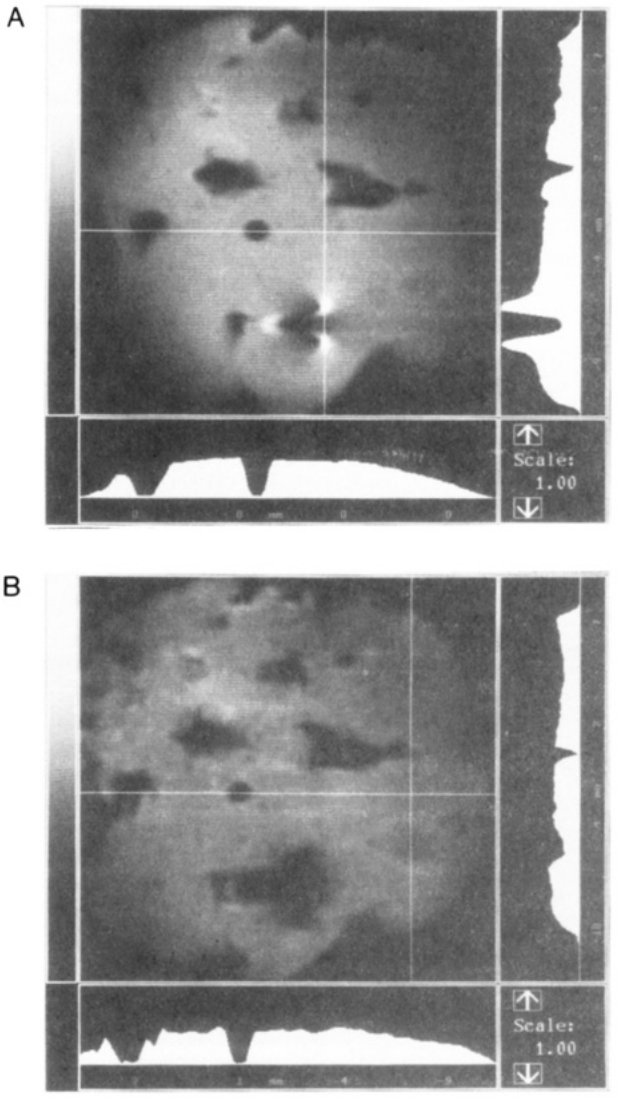

Figure 8. (A) Typical spin-echo, volume image slice of a phantom containing a capillary filled with air (top right), a capillary filled with powdered carbon black (close to center), a graphite pencil tip (lower center), and air pockets visible as irregular defects in a vegetable shortening matrix. Powdered carbon black was mixed with the shortening in the top one-third of the volume. Note the arrowhead artifact around the pencil tip. (B) Gradient-echo image of the same slice. TE, 1.3 ms; TR, 1 s; total time, 1 h in both A and B.

gradient strength of 20 G/cm and a TE of about 1 ms, the T_2-weighted 3D images can readily differentiate *cis*-BR/SBR diblends which vary in molecular composition by about 20%. Tire treads having differences in carbon black mixing can be differentiated at medium (150-μm) resolution. Short echo times dramatically improve image quality, and the multislice 3D imaging sequence is a valuable approach for imaging real elastomeric composites, although T_2 weighting is still present in the images of common elastomers. Magnetic susceptibility artifacts frequently appear in the images of filled elastomers and may be a means for identifying various defects based on their magnetic susceptibility differences.

Acknowledgment. We thank Ken Schur of the Uniroyal–Goodrich Tire Co. for providing the samples and for stimulating discussions. We also thank Bob Kadunce of BF Goodrich Co. for valuable discussions of carbon black dispersion and Jim Visintainer of Goodyear Research for discussions about issues in tire characterization. We thank J. Ackerman and L. Garrido of Massachusetts General

Hospital for suggesting magnetic susceptibility differences as the cause of the arrowhead artifacts. We thank Annadell Fowler and John Pearce for running the ^{13}C and ^{1}H NMR spectra, respectively. This research was funded by Grant AFOSR-89-0418 from the Air Force Office of Scientific Research.

References and Notes

(1) Listerud, J. M.; Sinton, S. W.; Drobny, G. P. *Anal. Chem.* **1989**, *61*, 23A.
(2) Weisenberger, L. A.; Koenig, J. L. *Appl. Spectrosc.* **1989**, *43*, 1117.
(3) Clough, R. S.; Koenig, J. L. *J. Polym. Sci., Polym. Lett.* **1989**, *27*, 451.
(4) Sarkar, S. N.; Wooten, E. W.; Komoroski, R. A. *Appl. Spectrosc.* **1991**, *45*, 619.
(5) Dechter, J. J.; Komoroski, R. A.; Ramaprasad, S. *J. Magn. Reson.* **1991**, *93*, 142.
(6) Garrido, L.; Ackerman, J. L.; Ellingson, W. A. *J. Magn. Reson.* **1990**, *88*, 340.
(7) Chang, C.; Komoroski, R. A. *Macromolecules* **1989**, *22*, 600.
(8) Komoroski, R. A.; Sarkar, S. N. *Proc. Mater. Res. Soc.* **1991**, *217*, 3.
(9) Webb, A. G.; Jezzard, P.; Hall, L. D.; Ng, S. *Polym. Commun.* **1989**, *30*, 364.
(10) Blümler, P.; Blümich, B. *Macromolecules* **1991**, *24*, 2183.
(11) Miller, J. B. *Trends Anal. Chem.* **1991**, *10*, 59.
(12) Cory, D. G.; Miller, J. B.; Turner, R.; Garroway, A. N. *Mol. Phys.* **1990**, *70*, 331.
(13) Cory, D. G.; deBoer, J. C.; Veeman, W. S. *Macromolecules* **1989**, *22*, 1618.
(14) Frahm, J.; Merboldt, K. D.; Hanicke, W. *J. Magn. Reson.* **1987**, *72*, 502.
(15) Komoroski, R. A. In *High Resolution NMR Spectroscopy of Synthetic Polymers in Bulk*; Komoroski, R. A., Ed.; VCH Publishers: Deerfield Beach, FL, 1986; Chapter 4.
(16) Lee, S. W.; Hilal, S. K.; Cho, Z. H. *Magn. Reson. Imaging* **1986**, *4*, 343.
(17) Chang, C.; Komoroski, R. A. In *Solid State NMR of Polymers*; Mathias, L. J., Ed.; Plenum: New York, 1991; in press.
(18) Chu, S. C.-K.; Xu, Y.; Balschi, J. A.; Springer, C. S., Jr. *Magn. Reson. Med.* **1990**, *13*, 239.
(19) Ludeke, K. M.; Roschmann, P.; Tischler, R. *Magn. Reson. Imaging* **1985**, *3*, 329.
(20) Kadunce, R. *Rubber Chem. Technol.* **1974**, *47*, 469.
(21) Komoroski, R. A. *Rubber Chem. Technol.* **1983**, *5*, 959.
(22) Komoroski, R. A.; Mandelkern, L. In *Applications of Polymer Spectroscopy*; Brame, E. G., Ed.; Academic Press: New York, 1987; Chapter 5, p 57.
(23) Jezzard, P.; Carpenter, T. A.; Hall, L. D.; Jackson, P.; Clayden, N. J. *Polym. Commun.* **1991**, *32*, 74.
(24) Vegvari, P. C.; Hess, W. M.; Chirico, V. E. *Rubber Chem. Technol.* **1978**, *51*, 817.
(25) Kadunce, R. J.; Smith, R. W. In Proceedings of the International Symposium for Testing and Failure Analysis, Los Angeles, Nov 9–13, 1987 (sponsored by ASM International, Metals Park, OH).